Relativistic Density Functional Calculations of EPR *g* Tensor for $\eta^1\{CuNO\}^{11}$ Species in Discrete and Zeolite-Embedded States

Piotr Pietrzyk[†] and Zbigniew Sojka*[,†,‡]

Faculty of Chemistry, Jagiellonian University, Ingardena 3, 30-060 Cracow, Poland, and Regional Laboratory of Physicochemical Analyses and Structural Research, Ingardena 3, 30-060 Cracow, Poland

Received: May 20, 2005; In Final Form: September 5, 2005

Spin-unrestricted zeroth order regular approximation (ZORA) and the scalar relativistic method based on Pauli Hamiltonian implemented in the Amsterdam Density Functional suite were used to calculate the electronic ***g*** tensor for isolated covalent $\{CuNO\}^{11}$ and electrostatic $\{q\text{-}NO\}^1$ species and for various model molecular and nonmolecular $\{CuNO\}^{11}$-containing systems, epitomizing copper nitrosyl cage adducts in the ZSM-5 zeolite. The predicted ***g*** tensor values using the ZORA/VWN scheme were in satisfactory agreement with experimental EPR results. Relativistic, diamagnetic, and paramagnetic contributions to the calculated ***g*** tensor were quantified. The nature of the observed Δg shifts was discussed in terms of the molecular orbital contributions due to the magnetic field-induced couplings and their structure sensitivity. The influence of basis set and exchange-correlation functional on the results was also briefly evaluated.

1. Introduction

Paramagnetic copper nitrosyl adducts $\eta^1\{CuNO\}^{11}$ are the key intermediates implicated in many enzymatic and inorganic heterogeneous catalytic systems that are involved in environmentally important nitrogen oxide processes, such as global nitrogen cycles[1] or, in a more local scale, abatement of anthropogenic NO_x polutants.[2] In the latter context, CuZSM-5 zeolites have been found to be highly active for decomposition of nitric oxide into its constituents, providing an incentive for extensive studies focusing on the copper-nitrosyl intermediates by means of a variety of experimental and theoretical approaches.[3−6] In addition to the catalytic *de*NO_x reaction over CuZSM-5 zeolites, copper nitrosyls are also purported intermediates during the nitrite reductase in Cu-containing enzymes, whereby NO_3^- and NO_2^- ions are reduced to gaseous NO or N_2O.[7] Numerous copper proteins have been probed with NO, resulting in distinct chemical and spectroscopic changes related to the formation of the $\eta^1\{CuNO\}^{11}$ adducts and the nature of the copper−NO interactions.[8,9]

A crucial aspect of the reactivity of nitric oxide is its coordination to and activation by copper ions. For understanding the fundamental chemistry of the Cu−NO species, a molecular level description of its electronic and magnetic properties in discrete and embedded states are of great importance in order to control its reactivity through the judicious design of appropriate active centers.[5,6,10] Among the different spectroscopic techniques applied to investigation of the paramagnetic $\eta^1\{CuNO\}^{11}$ adducts, conventional X-band and, more recently, high field W-band CW-EPR as well as time dependent EPR techniques have been used.[11] However, an analysis and interpretation of the magnetic parameters in terms of the molecular structure of the $\eta^1\{CuNO\}^{11}$ unit is not a trivial task because of a complex nature of the electronic interactions involved and its low C_s symmetry, resulting in a noncoincidence of the principal axes of the ***g***, hyperfine (^{14}N, $I = 1/2$), and superhyperfine ($^{63,65}Cu$, $I = 3/2$) ***A*** tensors. Therefore, taking the available experimental EPR parameters as computational targets, those data may be further analyzed in detail by the appropriate quantum chemical calculations. A successful reproduction of the ***g*** and ***A*** tensors, in turn, can be taken as an austere verification of the adequacy of the adopted model and the computational approach, providing a quantitative connection between the detailed molecular structure of the investigated paramagnet and its spectroscopic fingerprints.

The early theoretical studies of the EPR ***g*** tensor can be traced back to the well-known work of Stone, who derived his sum-over-states (SOS) theory.[12] In conjunction with the extended Hückel method, it was widely used, i.e., to interpret ***g*** tensors of many transition-metal complexes.[13] More recent and accurate ab initio approaches based on the multireference configuration interaction MRCI[14] and multiconfiguration self-consistent-field MCSCF[15] methodologies are largely restricted to the radicals or systems composed of light elements, because inclusion of all perturbation operators relevant for the electronic ***g*** tensor at the Breit-Pauli treatment of the spin−orbit coupling is computationally quite expensive. For larger systems containing transition-metal ions density functional theory (DFT), which approximately includes the electron correlation and exchange, owing to recent developments in the relativistic theory of the ***g*** tensor provides an attractive alternative.[16] There are several DFT implementations of the ***g*** tensor calculations reported in the literature, which basically fall into two major classes. Two-component approaches (ZORA in ADF[17] and Douglas-Kroll in PARAGAUSS[18]) include spin−orbit coupling treated variationally with the ***g*** tensor calculated as a first-order property. In one-component methods (Pauli in ADF,[19] deMon-EPR,[20] ORCA[21]), both magnetic field and spin−orbit coupling are treated as perturbations, leading to the second-order ***g*** tensor expression. In larger systems, the gauge dependence of the ***g*** tensor may

* Corresponding author tel.: +48 12 663 22 95; fax: +48 12 634 05 15; e-mail: sojka@chemia.uj.edu.pl. Corresponding author address: Faculty of Chemistry, Jagiellonian University, ul. Ingardena 3, 30-060 Cracow, Poland.

† Jagiellonian University.

‡ Regional Laboratory of Physicochemical Analyses and Structural Research.

10.1021/jp0526501 CCC: $30.25
Published on Web 10/28/2005

become quite sensitive to the choice of the coordinates origin. Common approaches to cope with this problem include application of gauge-including atomic orbitals (GIAO) or individual gauge origin for localized orbitals (IGLO).[22]

In this paper we report the results of DFT calculations of the molecular structure and the $\boldsymbol{g}$ tensor of the bare $\eta^1\{CuNO\}^{11}$ unit, and $\eta^1\{CuNO\}^{11}$ embedded in various clusters epitomizing the host sites in ZSM-5 zeolite as well. The principal goal of the paper was to corroborate a previous semiempirical analysis of the experimental EPR spectrum and to reproduce the experimental $\boldsymbol{g}$ tensor. The influence of cluster size, basis set, various exchange-correlation functionals $\upsilon_{xc}[\rho]$, and the level of relativity treatment on the calculated $\Delta\boldsymbol{g}$ shifts was also examined. In view of the variety of environments the η^1-$\{CuNO\}^{11}$ moiety may reside in (multiple hosting sites in zeolite and proteins), and possible repercussion of such differences on spectral properties, we investigated structure sensitivity of the results of $\boldsymbol{g}$ tensor calculations more closely.

In this work, we apply the recently developed DFT implementation of the spin-unrestricted ZORA for calculation of the EPR $\boldsymbol{g}$ tensor to a closed-shell metal ion with paramagnetic ligand. To our knowledge, the intrazeolite $\eta^1\{CuNO\}^{11}$ZSM-5 adduct studied herein is the first large nonmolecular system, for which the $\boldsymbol{g}$ tensor calculations using such quantum chemical framework have been performed. It thus proffers a severe test for both the efficiency and the accuracy of the currently available calculation schemes, strengthened by the fact that copper is one of the most demanding elements for such calculations among the first-row transition metals.[23] Earlier DFT calculations of the $\boldsymbol{g}$ tensor have been restricted to a minimal $[Cu-NO]^+$ model and carried out within the restricted open-shell Kohn−Sham approximation, using the Douglas-Kroll decoupling scheme.[5] Unfortunately, because of the lack of EPR data for such systems, the calculated $\boldsymbol{g}$ tensor could not be directly compared with experiment.

2. Theoretical and Computational Approach

For the interpretation of EPR spectra within the spin-Hamiltonian formalism the $\boldsymbol{g}$ tensor parametrizes the interaction between an effective spin $\boldsymbol{S}$ of the paramagnet of interest and the external magnetic field $\boldsymbol{B}$. The resultant electronic Zeeman term H^Z may be written as

$$H^Z = 1/(2c)\boldsymbol{B}\cdot\boldsymbol{g}\cdot\boldsymbol{S} \tag{1}$$

The components of the $\boldsymbol{g}$ tensors can be obtained as formal second derivatives of the total energy E of the system, $g_{pq} = 1/\mu_B\, \partial^2 E/\partial \boldsymbol{B}_q \partial \boldsymbol{S}_p|_{B=S=0}$, in one component approach or as a first-order molecular property in two component methods. Conventionally, the $\boldsymbol{g}$ tensor can be factorized into a scalar free electron (g_e) and a 3×3 matrix part $\Delta\boldsymbol{g}$, containing spin−orbit coupling and other relevant contributions

$$\boldsymbol{g} = g_e\mathbf{1}_3 + \Delta\boldsymbol{g} \tag{2}$$

where $g_e = 2.0023192778$ is the free electron value, and $\mathbf{1}_3$ is the unit matrix. Such a form conveys the fact that $\Delta\boldsymbol{g}$ reflects spatially dependent shifts induced by various perturbations in bound atomic and molecular environments relative to the free electron reference.

For the theoretical treatment of the $\boldsymbol{g}$ tensor, accounting for the relativity within the zeroth order regular approximation (ZORA) to the Dirac equation, using an auxiliary function $K = [1 - V/2c^2]^{-1}$, the Zeeman Hamiltonian H^Z written in atomic units assumes the form

$$H^Z = g_e/(2c)[K/2\ \sigma\cdot\boldsymbol{B} + K/4\ \boldsymbol{B}\cdot\boldsymbol{L} + \boldsymbol{B}\cdot\boldsymbol{L}\ K/4 + \sigma\cdot(\nabla K/2 \times \boldsymbol{A})] \tag{3}$$

with $\boldsymbol{L} = \boldsymbol{r}\times\boldsymbol{p}$, σ standing for the Pauli spin matrices and c the velocity of light. The first term is the electron spin Zeeman term, the next two terms form the orbital Zeeman interaction, and the last term is the spin−orbit gauge correction. In the two component ZORA approach (available in the ADF package and used in this work), taking that a Kramers doublet Φ_1, Φ_2 completely determines magnetic properties, the components of $\boldsymbol{g}$ tensor are obtained from the matrix elements: $g_{kx} = 4c\mathrm{Re}\Phi_{12}{}^k = 4c\mathrm{Re}\Phi_{21}{}^k$, $g_{ky} = -4c\mathrm{Im}\Phi_{12}{}^k = 4c\mathrm{Im}\Phi_{21}{}^k$, $g_{kz} = 4c\mathrm{Re}\Phi_{11}{}^k = 4c\mathrm{Re}\Phi_{22}{}^k$, where $\Phi_{ij}{}^k = \langle\Phi_i|\partial H^Z/\partial B_k|\Phi_j\rangle$. For more details the reader is referred to the original literature.[17]

The alternative one-component method for $\boldsymbol{g}$ tensor calculations used here is due to Schreckenbach and Ziegler,[19] also implemented in the ADF suite. In this formulation of the $\boldsymbol{g}$ tensor, scalar relativistic effects are included in the quasi-relativistic framework employing frozen core orbitals in conjunction with the first-order Pauli Hamiltonian

$$H^{Pauli} = V + p^2/2 - p^4/(8c^2) + \nabla^2 V/(8c^2) + 1/2\ \sigma\cdot\mathbf{B} + 1/(4c^2)\sigma\cdot(\nabla V\times\boldsymbol{p}) = h^{nr} + h^{mv} + h^{Dar} + h^Z + h^{so} \tag{4}$$

retaining in addition to the spin Zeemen operator h^Z only nonrelativistic h^{nr}, mass-velocity h^{mv}, and Darwin h^{Dar} operators. The resultant $\boldsymbol{g}$ tensor can be then expressed in terms of several contributions

$$\Delta g_{st} = \Delta g^{rel}{}_{st} + \Delta g^{d}{}_{st} + \Delta g^{p}{}_{st} \tag{5}$$

where $\Delta g^{rel}{}_{st}$ combines scalar relativistic corrections, whereas the terms $\Delta g^{d}{}_{st}$ and $\Delta g^{p}{}_{st}$ stand for dia- and paramagnetic contributions to $\Delta\boldsymbol{g}$, respectively. The paramagnetic term ($\Delta g^{p}{}_{st}$) dominates the deviation of $\boldsymbol{g}$ tensor elements from the free electron value. It contains the contributions due to the frozen core ($\Delta g_{st}{}^{p,core}$), the magnetic field-induced coupling between occupied orbitals ($\Delta g_{st}{}^{p,occ-occ}$), and occupied and virtual orbitals ($\Delta g_{st}{}^{p,occ-virt}$) as well, the latter being usually the most important one.[24]

All single-point calculations of the $\boldsymbol{g}$ tensor were performed with the ADF[25−27] version 2004.01 program package using either local density (VWN) or gradient-corrected functionals (BP, BLYP, BPW91, PW91, PBE, revPBE, OLYP). As a standard the triple-ζ valence Slater-type orbital basis set plus a set of polarization functions (TZP) was used for all atoms, unless otherwise stated explicitly. The gauge dependence was solved by using GIAOs. Calculations of EPR parameters involved double group symmetry adopted functions and spin−orbit coupling included variationally to account for relativistic effects within the ZORA method.[17,28] The latest version of ADF allows for the spin-unrestricted calculations with the ZORA Hamiltonian within the so-called collinear approximation[29] that can account for the spin polarization, not included in two-component methods so far.

Geometry optimization was carried out by means of DMol[30] software developed by Accelrys Inc.[31] at the spin-unrestricted level with no symmetry restrictions, unless otherwise noted. While discussing one-electron energy level, we consider SOMO and LUMO terms in the sense of the highest occupied and the lowest unoccupied spin−orbital in the spin majority manifold, respectively. As the exchange-correlation potential we used the generalized gradient approximation (GGA) of Becke[32] and Perdew and Wang.[33] For structure dependence analysis a faster

scheme, employing a local spin density approximation (LSDA) with Vosko, Wilk, and Nusair exchange-correlation functional[34] was used. In all geometry optimizations a double numerical basis set supplemented by polarization functions (DNP) was used.

Zeolite centers hosting the copper−nitrosyl unit were modeled using clusters of various numbers of **T**-atoms (with **T** = Si or Al), to evaluate the importance of lateral geometric and electronic interactions with the zeolite framework acting as a rigid multidentate macroligand. $\{CuNO\}^{11}[Si_5AlO_6(OH)_{12}]$ (**Z6** site), $\{CuNO\}^{11}[Si_4AlO_5(OH)_{10}]$ (**M5(7)** site), and $\{CuNO\}^{11}$-$[Si_2AlO_2(OH)_8]$ clusters (**I2** site) were optimized within C_1 symmetry, whereas in the case of auxiliary $\{CuNO\}^{11}[Si_2AlO_2$-$(OH)_2H_6]$ and $\{CuNO\}^{11}[Al(OH)_4]$ clusters, denoted as **I2′** and **I1** respectively, a C_s symmetry was imposed (all those species will be collectively labeled hereafter as $\{CuNO\}^{11}$/Z). In addition to the embedded systems, four congener molecular complexes of the $\{CuNO\}^{11}L_n$ type with the pliant aqua and hydroxyl ligands, $\{CuNO\}^{11}(OH)$, $\{CuNO\}^{11}[(H_2O)_2]$, $\{CuNO\}^{11}$-$[(OH)(H_2O)]$, and $\{CuNO\}^{11}[(OH)(H_2O)_2]$, were used to model the influence of the coordination state on the calculated ***g*** values. The $\{CuNO\}^{11}$ unit both in bare and coordinated states was fully optimized using analytical gradients, while the zeolite embedded **Z6**, **M5(7)**, and **I2** states were optimized with constraints imposed on the terminal hydrogen atoms. Details on the geometry optimization and geometrical embedding scheme for zeolite clusters were reported in our previous study on the calculations of the hyperfine coupling constants (HFCCs) for those systems.[6]

3. Results and Discussion

3.1. Investigated Structures and Optimized Geometries. The Cu^+ ions in the ZSM-5 zeolite can be accommodated within the main channels (sites **M5**−**7**, constituted by five-, six-, and seven-membered rings), sinusoidal channels (four-, five-, and six-membered sites **Z4**−**6**), and within the intersections of both channels (sites **I2** and **I3** with 2-fold and 3-fold coordination, respectively). Following the works of Sauer et al.,[10,35] the **I2** and the **M7** sites are the most stable and plausibly are associated with two types of copper nitrosyl species, recently detected in the CuZSM-5 zeolite by means of multifrequency (X-, Q-, and W-band) EPR investigations.[36,37] The **M7** site contains two joint five-membered rings, where three out of seven **T** atoms are common and can therefore be considered as a more robust version of the simpler five-membered center **M5**, hereafter labeled as **M5(7)**. Such a truncation has been justified in our earlier[6] and other papers.[38,39] In our calculations the **M5(7)** site was epitomized by the $[Si_4AlO_5(OH)_{10}]^-$ cluster with Al in the T1 position. The **I2** center was modeled using the $[Si_2AlO_2(OH)_8]^-$ and $[Si_2AlO_2(OH)_2H_6]^-$ clusters with the Al atom placed in the T6 position, while for the **Z6** site (located in a zigzag channel) we used the $[Si_5AlO_6(OH)_{12}]^-$ cluster with Al in the T4 position. Despite being rather rudimentary, they were successfully used to investigate the electronic and molecular structure of various transition-metal ions hosted in zeolites.[40−42]

Coordination of a NO molecule to copper led to a bent η^1-*N* adduct in accordance with experiment.[36] The optimized geometries of the isolated $\eta^1\{CuNO\}^{11}$ and the coordinated η^1-$\{CuNO\}^{11}L_n$ systems in the spin doublet state are shown in Figure 1a−e. The Cu−N and N−O bonds as well as the Cu−N−O angle (α) were found to be quite sensitive to the coordination environment. Generally, upon addition of the coligands decrease of the bond length d_{Cu-N} and increase of both the d_{N-O} distance and the α angle with respect to the values

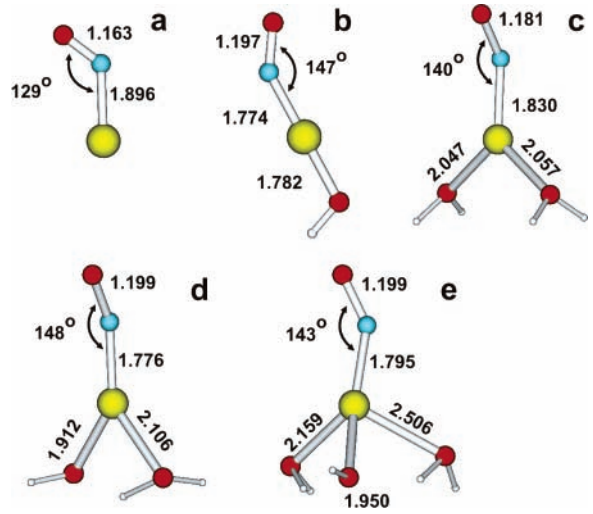

Figure 1. Optimized BPW/DNP structures and coordination of the bare $\eta^1\{CuNO\}^{11}$ and $\eta^1\{CuNO\}^{11}[OH(H_2O)_n]$ complexes. All bond lengths are given in angstroms, and angles, in degrees.

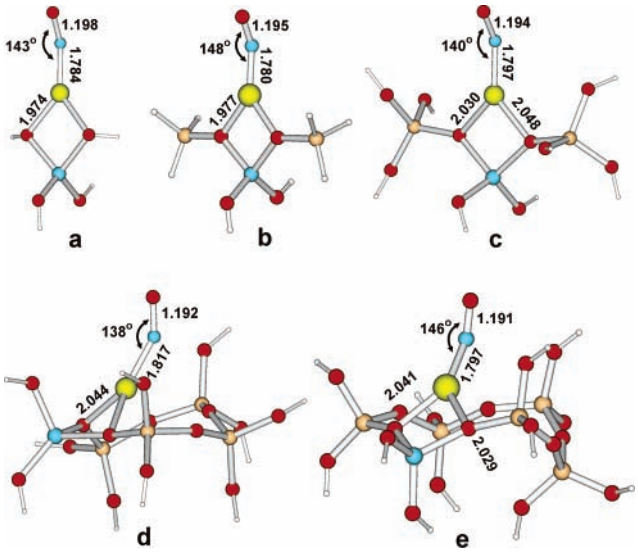

Figure 2. Optimized BPW/DNP structures of the embedded η^1-$\{CuNO\}^{11}$ unit within the framework of the ZSM-5 zeolite modeled with clusters of various size and location: (a) **I1**, (b) **I2′**, (c) **I2**, (d) **M5(7)**, and (e) **Z6**. All bond lengths are given in angstroms, and angles, in degrees.

in the bare $\eta^1\{CuNO\}^{11}$ unit were observed. Specifically, the geometry varied from $d_{Cu-N} = 1.890$ Å and α = 129° for η^1-$\{CuNO\}^{11}$ to $d_{Cu-N} = 1.774(6)$ Å and α = 147(8)° found in two complexes with the OH^- ligand. The average copper−nitrogen distance, $\langle d_{Cu-N}\rangle = 1.814$ Å, was distinctly smaller than the copper−aqua, $\langle d_{Cu-aq}\rangle = 2.175$ Å, and the copper−hydroxyl, $\langle d_{Cu-OH}\rangle = 1.881$ Å, bond lengths. Tilting of NO is a general phenomenon observed before and has been interpreted in terms of an increased $d_{z^2}-2\pi^*$ interaction.[43] The angle α was considerably greater for the OH^- containing species.

The structure of the nitrosyl complexes hosted in the zeolitic sites **I1**, **I2**, **I2′**, **M5(7)**, and **Z6**, shown in Figure 2a−e, repeated general trends (lengthening of the N−O bond, shortening of the Cu−N bond, and opening of the Cu−N−O angle) observed for the $\eta^1\{CuNO\}^{11}L_n$. The structural modifications of the $\{CuNO\}^{11}$ unit were greater the smaller the hosting cluster. For the C_1-optimized clusters **I2**, **M5(7)**, and **Z6**, the $NO-Cu(O_z)_2$ moiety exhibited a nearly C_s local symmetry with the mirror plane bisecting the angle δ_{O-Cu-O}, defined by the bonds between

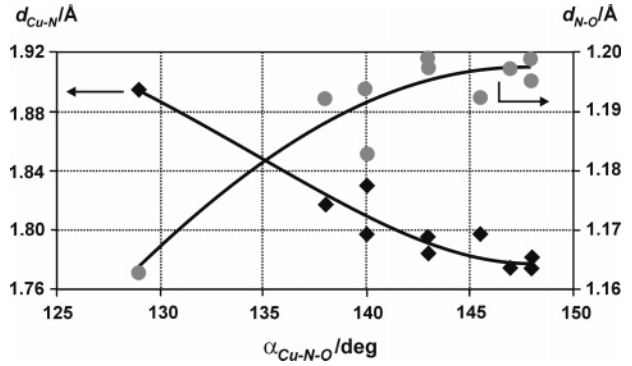

Figure 3. Mutual correlation for the optimized structures between the Cu−N−O angle (α) and the copper−nitrogen (d_{Cu-N}) and nitrogen−oxygen (d_{N-O}) bond lengths.

Cu and both proximal O_z{Al,Si} atoms (Figure 2c−e). The departure of the NO ligand from such a plane was smaller than 10°. The concomitant slight deformation of the Cu bonding to the framework consisted mainly in an appreciable contraction of the O_z-Cu-O_z angle in comparison to the unconstrained η^1\{CuNO\}^{11}[$(H_2O)_2$], while the average Cu−O_z distance remained practically the same as d_{Cu-aq}, in contrast to the distinctly shorter d_{Cu-OH} bond length. The bidentate coordination of the Cu^+ ion to the framework (assignment of the coordination numbers was based on the Cu−O bond length criterion d_{Cu-O} < 2.5 Å) exhibited nearly equal Cu−O_z bond lengths with $\langle d_{Cu-O}\rangle$ = 1.974(7) Å for H-terminated clusters **I1** and **I2′**, and $\langle d_{Cu-O}\rangle$ = 2.05(5) Å for clusters terminated with OH groups (**I2**, **M5(7)**, and **Z6**). Noteworthy, the geometrical parameters remained in a good agreement with the results of earlier calculations.[35,38] More information about the structure and bonding of NO to copper can be found in earlier papers.[6,10]

For all investigated copper nitrosyl systems there is an apparent correlation between the Cu−N bond length d_{Cu-N} and the Cu−N−O bond angle α as shown in Figure 3. The lower the angle α, the shorter is the distance d_{Cu-N} and simultaneously the longer the N−O bond length d_{N-O}. This indicates that nitric oxide activation (expressed as the N−O bond lengthening) is accompanied by shortening of the Cu−N distance. Similar changes were previously observed for various cobalt dioxygen adducts by Boca and discussed elsewhere in more detail.[44]

3.2. Selection of Correlation-Exchange Functional and Basis Set. One of the major problem in calculating magnetic parameters is proper description of the electron-correlation effects. This motivated us to a detailed examination of the influence of $v_{xc}[\rho]$ functionals on the calculated ***g*** tensor, using the minimal model η^1\{CuNO\}^{11} and the TZP basis set as a standard scheme for this purpose. The performance of several approximate density functionals including two local, VWN and Stoll-VWN, as well as several gradient-corrected BP86, BLYP, BPW91, PW91, PBE, revPBE, and OLYP functionals was examined. The latter generally tend to be more accurate than VWN for many other molecular properties, but in the case of the ***g*** tensor they may give comparable result. This is valid for main-group radicals[45] and for some transition-metal complexes as well.[46]

The evaluation study revealed that the calculated g_{xx} and g_{yy} values showed only a marginal dependence on the specific functional. The only substantial deviation was observed for the g_{zz} component in the case of VWN. All the investigated GGA functionals gave very close results for all ***g*** tensor values, and it was essentially not possible to select one that would be superior to the others. Similar behavior was previously observed and discussed for d^1 complexes.[46] For further calculations we selected the local VWN and the gradient-corrected BPW91 density functionals. The choice of the latter was supported by the fact that it was also the most advantageous in previous hyperfine coupling constant calculations for the same copper nitrosyl adducts.[6]

TABLE 1: Effect of the Basis Set on the Spin-Unrestricted ZORA Collinear *g* Tensor Calculations[a]

basis set	g_{xx}	g_{yy}	g_{zz}
SZ	1.4334	2.4260	1.0900
DZ	2.0106	2.0169	1.9062
TZP	2.0110	2.0158	1.9156
TZ2P	2.0108	2.0155	1.9198
QZ4P	2.0121	2.0117	1.9205

[a] Data for the η^1\{CuNO\}^{11}/**I2** complex.

As pointed out by Schreckenbach and Ziegler,[19] the ability of the DFT calculations to reproduce correctly the values of EPR ***g*** tensor depended on the basis sets variety. Therefore we tested the convergence of single-ζ (SZ) and double-ζ (DZ) as well as triple-ζ basis sets. The latter were augmented with one set of polarization functions (TZP) or two sets of polarization functions (TZ2P). Additionally quadruple-ζ 4P (QZ4P) was also used. The results obtained for the **I2** cluster are summarized in Table 1. While analyzing these data, it should be noted that the precision of the experimental ***g*** tensor is limited to three digits after the decimal point, especially for the partially overlapped g_{xx} and g_{yy} components. Thus changes of ±0.001 or less in the calculated values between two basis sets can reasonably be considered as practically insignificant.[46] Bearing this in mind, from the inspection of Table 1, we can readily deduce that SZ and DZ are not sufficient, whereas the triple-ζ sets (TZP and TZ2P) give almost similar results, although taking into account the performance of QZ4P, they are probably not fully converged. The largest deviation between TZP and more accurate TZ2P was observed for the g_{zz} component. However, the resultant error is small as compared to the deviation between theory and experiment. We can thus infer that the TZP basis is sufficient to draw meaningful conclusions from the calculated ***g*** tensor shifts.

3.3. EPR *g* Tensor of Discrete η^1\{CuNO\}^{11} Unit. Due to the limitations of the currently available computation methodologies it is not easy to construct a very accurate model for calculation of the ***g*** tensor for such a complicated system as the η^1\{CuNO\}^{11} unit embedded in ZSM-5, considered here. Conceptually useful results can be achieved already by analyzing simpler models that can be next embedded into the broad range of conceivable chemical environments with pliant (complexes, enzymes) or rigid (zeolitic framework) ligands. The common feature of such paramagnets is large confinement of the spin density distribution within the η^1\{CuNO\}^{11} moiety. As a result, it bears a dominant part of the magnetic properties of the whole system; therefore, for the sake of further discussion, it can be termed a ***magnetophore***, in analogy to chromophore in the optical spectroscopy.

To get some insight into its electronic nature, the ***g*** tensor was first calculated for the bare covalent η^1\{CuNO\}^{11} and a related purely electrostatic $\eta^1\{q-NO\}^1$ species. In the latter case, the DFT results can be compared with the simple semiempirical treatment developed originally for the O_2^- ($^2\Pi_{3/2}$) species by Känzing and Cohen,[47] which has been widely used also for analysis of the ***g*** tensor of the bound nitric oxide.[36,48]

In a NO molecule ($\sigma^2\pi^4\pi^{*1}$), the unpaired electron occupies the antibonding $\pi^*(2p)$ orbital giving rise to the $^2\Pi_{1/2}$ ground state. Because the spin and the orbital magnetic moments that

TABLE 2: Calculated *g* Tensor Values for the $\eta^1\{CuNO\}^{11}$ Magnetophore in Various Environments within Spin-Unrestricted Collinear ZORA and Scalar Pauli Approximations[a]

structure	method	g_{xx}	g_{yy}	g_{zz}	noncoincidence angle β/deg
		Discrete State $\eta^1\{q-NO\}^1$ and $\eta^1\{CuNO\}^{11}$			
$\{q-NO\}^1$	ZORA/VWN	2.0007	2.0065	1.8869	
	scalar Pauli	2.0019	2.0070	1.8835	
	eq 6	1.9960	2.0005	1.9145	
$\{CuNO\}^{11}$	ZORA/VWN	2.0071	2.0109	1.9580	22.0
	ZORA/BPW91	2.0055	2.0092	1.9690	13.1
	scalar Pauli	2.0075	2.0113	1.9585	
	DK[5]	2.0074	2.0123	1.8668	
		Coordinated State $\eta^1\{CuNO\}^{11}$			
$\{CuNO\}^{11}(OH)$	ZORA/VWN	1.9997	2.0101	1.8709	40.7
$\{CuNO\}^{11}[(OH)(H_2O)]$	ZORA/VWN	2.0035	2.0113	1.9062	
$\{CuNO\}^{11}[(H_2O)_2]$	ZORA/VWN	2.0081	2.0154	1.9158	
$\{CuNO\}^{11}[(OH)(H_2O)_2]$	ZORA/VWN	2.0099	2.0143	1.8821	
$\{CuNO\}^{11}/[Al(OH)_4]$	ZORA/VWN	2.0109	2.0115	1.9130	40.0
	ZORA/BPW91	2.0073	2.0102	1.9390	39.6
		Embedded State $\eta^1\{CuNO\}^{11}$			
$\{CuNO\}^{11}$/**I2′**	ZORA/VWN	2.0061	2.0113	1.8895	47.4
	scalar Pauli	2.0077	2.0120	1.8872	
$\{CuNO\}^{11}$/**I2**	ZORA/VWN	2.0110	2.0158	1.9156	
	ZORA/BPW91	2.0102	2.0108	1.9422	
	scalar Pauli	2.0117	2.0171	1.9136	
$\{CuNO\}^{11}$/**M5(7)**	ZORA/VWN	2.0112	2.0191	1.9041	
	ZORA/BPW91	2.0106	2.0139	1.9335	
	scalar Pauli	2.0125	2.0205	1.9015	
$\{CuNO\}^{11}$/**Z6**	ZORA/VWN	2.0082	2.0117	1.8806	
	scalar Pauli	2.0095	2.0137	1.8775	
		Experimental Values			
$\{CuNO\}^{11}$/ZSM-5	X-band EPR [36]	2.000	2.003	1.889	40
	W-band EPR [37]	2.005	2.005	1.891	35
	W-band EPR [37]	2.005	2.005	1.917	35

[a] In the case of C_s symmetry the noncoincidence angle (β) between ***g*** and $^{Cu}\boldsymbol{A}$ tensors is additionally given.

are antiparallel almost cancel, this state is efficiently nonmagnetic, and no EPR signal could be observed unless the degeneracy of both π^* orbitals, $\pi_x^* = 1/\sqrt{2}(\pi^*_{-1} - \pi^*_1)$ and $\pi_y^* = i/\sqrt{2}(\pi^*_{-1} + \pi^*_1)$, is removed due to the interaction with the surrounding point charge q, resulting in quenching of the orbital magnetic moment.[48,49] In such a case the unpaired electron is assumed to be localized on one of the π^* orbitals, and the crystal field distortion $\Delta = <\pi_y^*|V_{CF}|\pi_y^*> - <\pi_x^*|V_{CF}|\pi_x^*>$ gives rise to two states with the energies equal to $1/2\lambda[1+ (\Delta/\lambda)^2]^{0.5}$, where $\lambda = 123$ cm^{-1} (0.015 eV) is the free-molecule spin−orbit coupling constant. Taking into account second-order contribution due to the promotion of an electron from the σ orbital to the π^* (E) the following formulas for the ***g*** tensor in terms of λ, Δ, and E parameters are obtained[50]

$$g_{zz} = g_e - 2l\sin2\alpha$$

$$g_{yy} = g_e\cos2\alpha + (\lambda/E)(1 + \cos2\alpha + \sin2\alpha)$$

$$g_{xx} = g_e\cos2\alpha + (\lambda/E)(\cos2\alpha - \sin2\alpha - 1) \qquad (6)$$

where $\tan2\alpha$ is defined as λ/Δ and $l = i <\pi_y^*|L_z|\pi_x^*>$. From these equations it follows that $g_{yy} \sim g_{xx} > g_{zz}$ and the only important shift from the g_e value is expected for the g_{zz} component, as experimentally observed indeed.

In Table 2 the EPR ***g*** tensors calculated for the bare $\eta^1\{q-NO\}^1$ and $\eta^1\{CuNO\}^{11}$ magnetophores with various methods are collated. The energy values of Δ and E parameters appearing in eq 6 were taken from the ZORA DFT results. Unfortunately, no gas phase EPR data exist for those species to be directly compared with the calculated values. All the calculations reproduce the same sequence, $g_{zz} < g_{xx} < g_e < g_{yy}$ and $g_{zz} < g_e < g_{xx} < g_{yy}$, of the ***g*** tensor components for NO stabilized on q^+ and Cu^+ ion, respectively. The validity limit of the electrostatic model was further explored for the $\eta^1\{q-NO\}^1$ unit as a function of an angular deformation gauged by the value of the $q-N-O$ angle. Because of the very shallow potential energy surface, this is the most probable distortion mode.[5,35] The results were compared with spin-unrestricted ZORA DFT calculations for $\eta^1\{q-NO\}^1$ and $\eta^1\{Cu-NO\}^{11}$ and are shown in Figure 4. In the case of the $\eta^1\{q\text{-}NO\}^1$ species, within the range of $90° < \alpha < 140°$, the g_{zz} component was surprisingly well reproduced by the electrostatic model, and both treatments gave nearly the same results. However, for g_{yy} and especially for the g_{xx} component the agreement with the ZORA results appeared less satisfactory, and the calculated values derived from the electrostatic model were systematically underestimated (Figure 4b,c). The discrepancies between $\eta^1\{q-NO\}^1$ and $\eta^1\{CuNO\}^{11}$ species were most apparent for the g_{yy} and, to a lesser extent, for the g_{xx} component. This is caused by additional transitions, absent in $\eta^1\{q-NO\}^1$ species, that involve copper d-orbitals. In the case of g_{zz}, the shift is determined mainly by the SOMO-LUMO splitting and preserves its intraligand character (vide infra). However, for the angles $\alpha > 140°$, when SOMO-LUMO splitting approaches the spin−orbit coupling limit, the discrepancy between ZORA and the electrostatic model diverges quite dramatically.

3.4. EPR *g* Tensor of $\eta^1\{CuNO\}^{11}L_n$ and $\eta^1\{CuNO\}^{11}$/Z. In the previous section we restricted our discussion to the minimal models that completely neglect any molecular environment. This implies that one may not necessarily rely on such results with respect to the embedded states because interactions with the zeolite framework could alter the structure of the η^1-

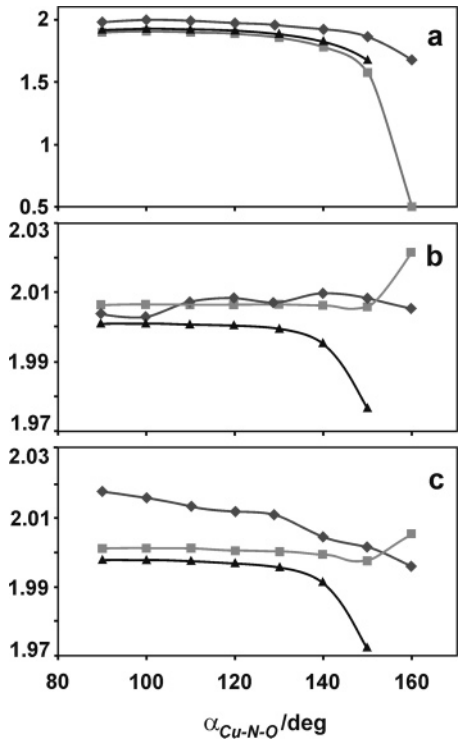

Figure 4. Dependence of the calculated $\boldsymbol{g}$ tensor components (a) g_{zz}, (b) g_{xx}, and (c) g_{yy} on the Cu−N−O bending angle (α) for the η^1-{CuNO}^{11} (-♦-), $\eta^1\{q\text{−NO}\}^1$ (-■-) (ZORA/VWN), and for the $\eta^1\{q\text{−NO}\}^1$ (-▲-) (electrostatic model) species.

{CuNO}^{11} magnetophore sufficiently enough to affect the very sensitive g_{zz} component notably.

Following the previous work[51] on calculation of hyperfine coupling constants, we examined copper nitrosyl complexes η^1-{CuNO}^{11}[(OH)$(H_2O)_n$] with an increasing number of water ligands. This allows for stepwise modeling of influence of the coordination environment on the particular components of the $\boldsymbol{g}$ tensor. Additionally, the cluster type models **I1**, **I2**, **I2′**, **M5-(7)**, and **Z6**, constituting a more realistic representation of the molecular surroundings of the copper center in the zeolite channels, were investigated. The results of the calculations are summarized in Table 2.

As it can be seen, the calculated g_{xx} and g_{yy} components were relatively insensitive to the choice of the molecular geometries, with the variation range of the g_{yy} value (0.005) being smaller twice than that of g_{xx} one (0.010). Addition of an axial OH ligand of the π-donor character led to significant changes in the geometry of the Cu−NO moiety (Figure 1b), which was reflected in a substantial negative shift of the g_{zz} value with respect to the isolated state. The influence of weaker aqua ligands was less pronounced, and it consisted of partial compensation of the large Δg_{zz} shift induced by the coordinated hydroxyl. For the η^1-{CuNO}^{11}[(OH)$(H_2O)_2$] complex, a probably fortuitous good match with the experimental values was obtained (Table 2), despite that the coordination number of copper in this structure is not compatible with that postulated in the ZSM-5 zeolite.

The magnetic parameters of the η^1-{CuNO}^{11} unit embedded in the zeolitic sites repeated previous conjectures concerning the influence of the cluster type on the particular g_{ii} components. Interestingly, the ZORA results obtained with the local VWN (and also the scalar Pauli approximation data) appeared to be distinctly superior to those calculated with gradient-corrected BPW91 functional. Generally, the calculated components were

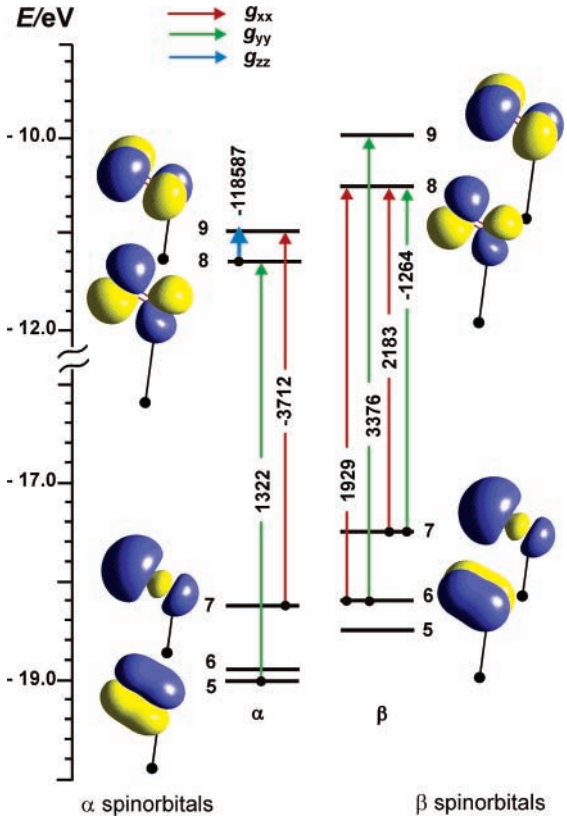

Figure 5. Molecular orbital diagram for the most important paramagnetic contributions to the $\boldsymbol{g}$ tensor components of the $\eta^1\{q\text{−NO}\}^1$ species in spin-unrestricted VWN/TZP scalar relativistic calculations based on Pauli Hamiltonian. The magnetic field-induced couplings of MOs are indicated with arrows, and the corresponding contributions in ppm (>10%) are also given. The individual molecular orbitals are identified by the side view of the corresponding contours.

systematically slightly greater compared to experiment. A similar effect observed previously for d^1 systems has been assigned to overestimation of the covalent character of bonds formed by metal d orbitals.[46] We can readily infer from Table 2 that the ZORA/VWN and scalar Pauli methods are both able to reproduce the $\boldsymbol{g}$ tensor components of the η^1-{CuNO}^{11}/ZSM-5 quite satisfactorily. Two distinct values of $g_{zz} = 1.916$ obtained for the **I2** sites and g_{zz} around 1.89 for **M5(7)** and **Z6** to be compared to $g_{zz} = 1.917$ and $g_{zz} = 1.891$ from experiment, respectively, account quite well for the observed speciation of the copper nitrosyl cage adducts. The validity of the **M5(7)** model is additionally reinforced by the fact that it gave rise to correct ^{63,65}Cu and ^{14}N hyperfine coupling constants as well.[6]

3.5. Molecular Nature of $\boldsymbol{g}$ Tensor. The analysis of individual contributions to the Δg values according to eq 5 was performed using the results of relativistic spin-unrestricted DFT calculations based on the scalar Pauli Hamiltonian, as developed by Schreckenbach and Ziegler.[19] Focusing our attention on g_{iso} at the beginning, the partitioning revealed that the paramagnetic term ($\Delta g_{st}^{p,occ-virt}$) largely dominates, accounting for more than 90% of the total shift for the $\eta^1\{q\text{−NO}\}^1$ and η^1-{CuNO}^{11}-related species (Table 3). The corrections due to relativistic effects (Δg_{iso}^{REL}) and magnetic field-induced coupling between occupied orbitals ($\Delta g_{iso}^{p,occ-occ}$), comparable in magnitude, are below 1% for $\eta^1\{q\text{−NO}\}^1$ and 3% for η^1-{CuNO}^{11}, whereas the diamagnetic corrections (0.2−0.6%) appear practically unimportant. Therefore, in getting a semiquantitative insight into the molecular origin of the $\boldsymbol{g}$ tensor, following earlier papers,[22]

TABLE 3: Contributions to the Δ*g* Tensor Arising from Relativistic Scalar Pauli Hamiltonian[a]

			Δg_{iso}^{p}		
structure	Δg_{iso}^{REL}	Δg_{iso}^{d}	$\Delta g_{iso}^{p,occ-occ}$	$\Delta g_{iso}^{p,occ-vir}$	gauge invariance
$\{q-NO\}^{1}$ [b]	−276	77	242	−38177	−16
	0.7%	0.2%	0.6%	98.4%	0.04%
$\{CuNO\}^{11}$	−247	65	298	−10023	−10
	2.3%	0.6%	2.8%	94%	0.09%
$\{CuNO\}^{11}[(OH)H_2O]$	−290	81	−37	−28740	−16
	1%	0.3%	0.1%	98.5%	0.05%
$\{CuNO\}^{11}/[Al(OH)_4]$	−298	83	−109	−23682	−17
	1.2%	0.3%	0.5%	97.9%	0.07%
$\{CuNO\}^{11}$/**I2′**	−298	84	22	−33157	−14
	0.9%	0.3%	0.07%	98.7%	0.04%
$\{CuNO\}^{11}$/**M5(7)**	−310	83	228	−23893	−11
	1.3%	0.3%	1%	97.4%	0.04%

[a] Results of the VWN spin-unrestricted calculations. All values are given in ppm and in %. [b] For α = 120°.

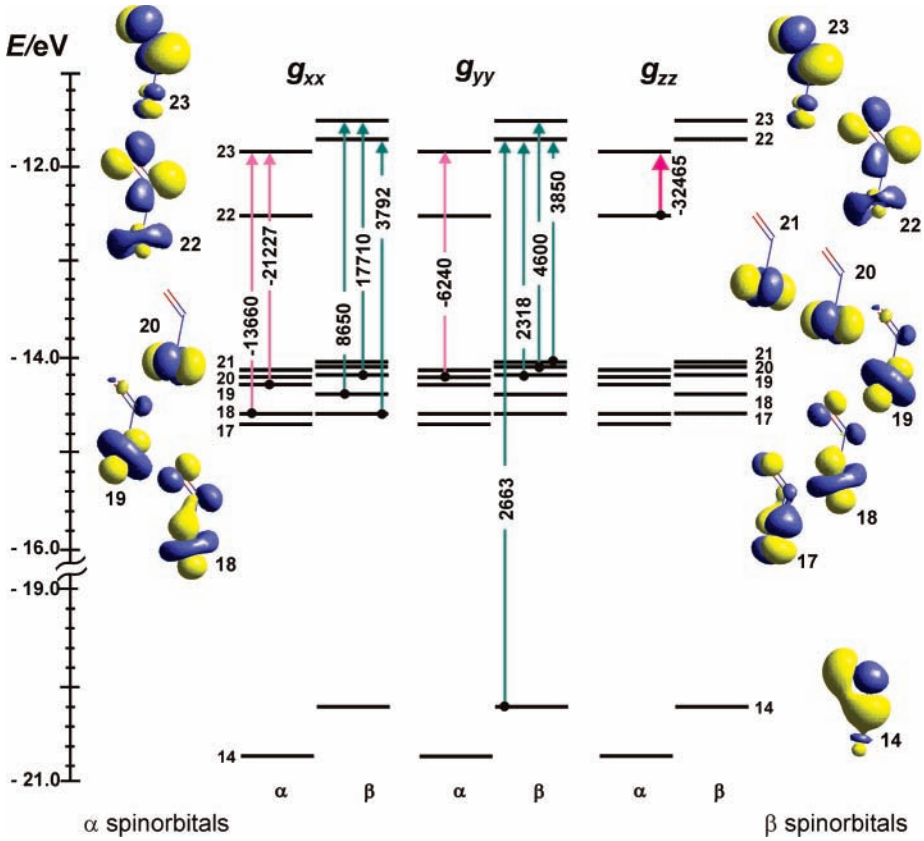

Figure 6. Molecular orbital diagram for the most important paramagnetic contributions to the ***g*** tensor components of the $\eta^1\{CuNO\}^{11}$ magnetophore in spin-unrestricted VWN/TZP scalar relativistic calculations based on Pauli Hamiltonian. The magnetic field-induced couplings of MOs are indicated with arrows, and the corresponding contributions in ppm (>10%) are also given. The individual molecular orbitals are identified by the side view of the corresponding contours.

we may reasonably confine our discussion to the overwhelming $\Delta g_{st}^{p,occ-virt}$ term, which primarily determines its main features.

The qualitatively most important contributions (exceeding 10% of the Δg_{iso}) to the ***g*** tensors of the $\eta^1\{q-NO\}^1$ and the $\eta^1\{CuNO\}^{11}$ magnetophores in the spin-unrestricted calculation scheme are depicted in Figures 5 and 6, together with the contours and the energies of the magnetically relevant molecular orbitals. In the case of the $\eta^1\{q-NO\}^1$ unit the shift of the g_{zz} component is determined by single coupling between the SOMO and the LUMO (α-8*a*′↔ α-9*a*″), and the contribution of this term is obviously negative. For the g_{xx} component three couplings are involved: α-7*a*′ ↔ α-9*a*″, *β*-6a″ ↔ *β*-8*a*′, and *β*-7*a*′ ↔ *β*-8*a*′. The α and the accumulated *β* contributions are of opposite sign but similar in magnitude, making the resultant positive paramagnetic shift of g_{xx} relatively small. The g_{yy} value, in turn, is determined by three couplings: α-5*a*′ ↔ α-8*a*′, *β*-6*a*″ ↔ *β*-9*a*″ and *β*-7*a*′ ↔ α-8*a*′. The Δg_{yy} shift has been essentially determined by the positive *β*-6*a*′ ↔ *β*-9*a*″ term, since the first and the last one nearly cancel. This provides molecular rational for the $g_{zz} < g_{xx} < g_{yy}$ sequence, which was experimentally observed in the cases where the electrostatic model is reasonably applicable.[48,50,52]

The situation becomes more complicated for the $\eta^1\{CuNO\}^{11}$ magnetophore because of the admixture of copper 3*d* orbitals (Figure 6) and covalent bonding between copper and nitric oxide. The coupling space spreading from 14*a*′ to 23*a*″ incorporates new magnetically important orbitals such as 19*a*′, 20*a*″, and 21*a*′, which have no counterparts in $\eta^1\{q-NO\}^1$.

Being of the same symmetry, the π_u (5a') and σ_g (7a') MO of the $\eta^1\{q\text{-NO}\}^1$ are now hybridized and admixed with copper $3d_{z^2}$, forming a low-lying 14a' bonding orbital of the η^1-$\{\text{CuNO}\}^{11}$. The 17a'' and 18a' MOs are the bonding variants of the LUMO and SOMO, respectively.

For the sake of further discussion the involved molecular orbitals can be divided into two main groups: ligand-based MOs and metal-based MOs. The g_{zz} component is again determined by single α-22a'(SOMO) ↔ α-23a''(LUMO) coupling; therefore, the corresponding matrix element for this contribution is largely dominated by the spin−orbit coupling on the ligand center. Both orbitals, however, contain a small, yet significant admixture of copper 3d (d_{z2}, d_{yz}, d_{xz}) and 4s AOs, which accounts well for an appreciable modification of the Δg_{zz} shift in comparison to the purely ionic $\eta^1\{q-\text{NO}\}^1$ case (Table 2), and the molecular nature of the copper hyperfine tensor as well.[6,36] The separation in energy of the α-22a' and α-23a'' orbitals for the $\{\text{CuNO}\}^{11}$ species is distinctly greater (Δ = 0.64 eV) than in the case of $\{q\text{-NO}\}^1$ with Δ = 0.35 eV. Although its effect on the Δg_{zz} is partially compensated by the enhanced spin−orbit coupling due to the involvement of the copper orbitals (λ_{Cu} = 852 cm^{-1} is much larger than λ_N = 76 cm^{-1} and λ_O = 151 cm^{-1}), the resultant shift is smaller than in the electrostatic case (vide Table 2). However, as it can be inferred from the comparison of the MO diagrams shown in Figures 5 and 6, a close correspondence between the molecular origin of the Δg_{zz} shift for both $\eta^1\{q-\text{NO}\}^1$ and $\eta^1\{\text{CuNO}\}^{11}$ species is still preserved. In contrast, the g_{xx} and g_{yy} components exhibit clearly different electronic origin, despite that the relevant shifts are apparently quite similar (Table 2). They are dominated by the couplings between the metal-centered and the ligand-centered orbitals (Figure 6), which can be regarded as a kind of charge-transfer contributions.[46] In the case of the g_{xx}, there are two pairs of such charge-transfer couplings (α,β)-18a' ↔ (α,β)-23a'', which are negative for α and positive for β currents, and β-17a'' ↔ β-22a' coupling with the positive outcome. In turn, the most important positive terms contributing to g_{yy} include β-21a' ↔ β-22a', β-14a' ↔ β-22a', and 19a' ↔ β-22a' along with paired (α,β)-20a'' ↔ (α,β)-23a'' couplings. Among them, only the intraligand β-14a' ↔ β-22a' coupling can be treated as a far analogue of the combined β-6a'' ↔ β-9a'' and β-7a' ↔ α-8a' terms in the $\{q-\text{NO}\}^1$ magnetophore. The resulting Δg_{xx} and Δg_{yy} shifts are distinctly greater than those observed for $\{q-\text{NO}\}^1$, but their compound electronic nature makes the qualitative interpretation rather involved in contrast to the g_{zz} component. The g_{xx} and g_{yy} values are essentially determined by the charge-transfer type couplings and lose entirely their correspondence with the appropriate intraligand terms appearing in the $\{q-\text{NO}\}^1$ species.

Orientation of the principal axes with respect to molecular framework is shown in Figure 7a,b. The g_{yy} and g_{zz} axes are located in the Cu−N−O plane, whereas the g_{xx} axis is perpendicular to this plane, in accordance with the C_s symmetry of this paramagnet. The deviation of the g_{zz} component from the direction of the N−O bond, equal to 26.7°, is caused by the involvement of the 3d orbitals of copper as it can be inferred from comparison with the purely electrostatic $\eta^1\{q-\text{NO}\}^1$ model, where the g_{zz} axis is oriented almost along the N−O direction. The noncoincidence angle θ = 2.4° was very close to that of θ = 2.2° recently found for the electrostatic $\eta^1\{\text{Na}-\text{NO}\}^1$ adduct in ZSM-5 zeolite.[5] The major transitions causing the tilting of the axes in the yz plane are α-22a' ↔ α-23a'' (g_{zz}) and α-20a'' ↔ α-23a'', β-14a' ↔ β-22a', β-19a' ↔ β-22a', β-20a'' ↔ β-23a'', and β-21a' ↔ β-22a' (g_{yy}), implying specific involvement of the copper $3d_z^2$ and $3d_{yz}$ orbitals.

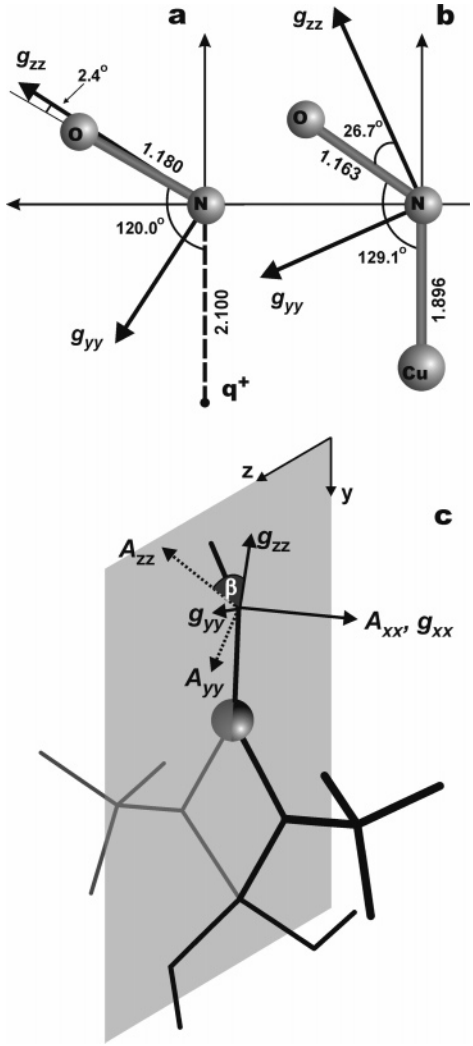

Figure 7. Principal directions of the ***g*** tensor axes with respect to the molecular framework of (a) $\eta^1\{\text{q-NO}\}^1$ and (b) $\eta^1\{\text{CuNO}\}^{11}$ species. (c) The noncoincidence angle (β) between the ***g*** and ^{Cu}***A*** tensor principal axes is shown for the $\eta^1\{\text{CuNO}\}^{11}$/**I2′** complex.

The modification of the molecular picture of the ***g*** tensor upon embedding was examined using again the $\eta^1\{\text{CuNO}\}^{11}$/**I2′** test species of the C_s symmetry (Figure 8). Two points are particularly worth mentioning here. In the case of the g_{zz} component, apart from the characteristic intraligand α-63a'-(SOMO) ↔ α-64a''(LUMO) term, an additional α-50a' ↔ α-64a'' coupling involving the framework ligand-based MO appeared. Although clearly less important than the dominant SOMO−LUMO interaction, it makes g_{zz} additionally sensitive to the nearest environment of copper, owing to large contributions of the framework orbitals to the 50a' MO.

The remaining g_{xx} and g_{yy} components of the $\eta^1\{\text{CuNO}\}^{11}$/**I2′** species are featured by multiplicity of the charge-transfer couplings. The relevant metal-based MOs contain sizable contributions from the framework-based orbitals (Figure 8). Specifically, the Δg_{yy} shift is determined by the outcome of a negative α-53a'' ↔ α-64a'' and two positive β-53a'' ↔ β-63a'' and β-55a' ↔ β-64a' contributions, whereas for the Δg_{xx} the relevant couplings are more abundant: α-54a' ↔ α-64a'', α-56a' ↔ α-64a'', and α-58a' ↔ α-64a'' as well as β-54a' ↔ β-63a'', β-56a' ↔ β-63a'', and β-58a' ↔ β-63a''. As a result, the nature

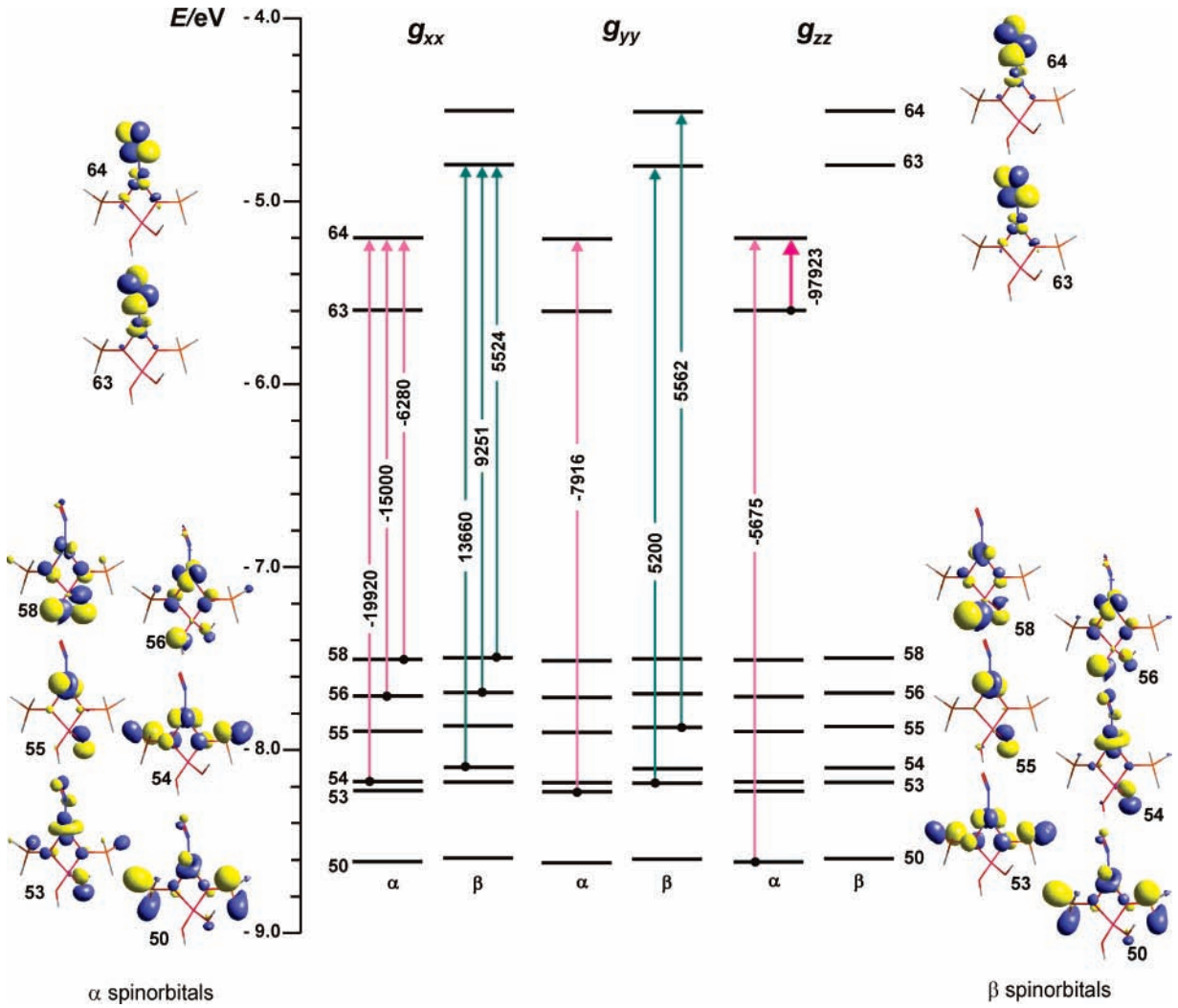

Figure 8. Molecular orbital diagram for the most important paramagnetic contributions to the ***g*** tensor components of the $\eta^1\{CuNO\}^{11}$/**I2′** complex in spin-unrestricted VWN/TZP scalar relativistic calculations based on Pauli Hamiltonian. The magnetic field-induced couplings of MOs are indicated with arrows, and the corresponding contributions in ppm (>10%) are also given. The individual molecular orbitals are identified by the side view of the corresponding contours.

of those components is rather complicated, and due to partial canceling they become effectively structure nondiagnostic (vide infra).

The low symmetry of the $\eta^1\{CuNO\}^{11}$/**I2′** species give rise to noncoincidence of the ***g*** tensor principal axes with respect to the $^{Cu}\boldsymbol{A}$ tensor and the molecular axes as well (Figure 7c). The calculated value of the noncoincidence angle $\beta = 41°$ remains in an excellent agreement with the experimental value $\beta = 40°$, derived from simulation of the EPR spectra of the $\eta^1\{CuNO\}^{11}$/ZSM-5 system.[36]

3.6. Sensitivity of *g* Tensor to Molecular Geometry. To explore further the structural diagnostic properties of the theoretically predicted ***g*** tensors, geometry sensitivity tests were performed for the most robust $\eta^1\{CuNO\}^{11}$/**M5(7)** cluster using the scalar Pauli Hamiltonian. As the variables to be examined we selected the metal−ligand bond length (d_{Cu-N}) in addition to the already mentioned Cu−N−O angle α (a commonly analyzed parameter because of the very shallow potential energy surface).[5,10,53] Systematic variation of these parameters (carried out separately) was followed by relaxation of the all remaining structural variables by partial optimization. The results of the calculations summarized in Figure 9 a,b confirmed that the g_{xx} and g_{yy} components are rather insensitive to both distortions in a broad range of their possible variations. Thus, the observed inaccuracies in predicting their values can most likely be connected with limitations of the available calculation schemes. Indeed, for transition-metal ion-containing systems an exact quantitative theoretical prediction of the ***g*** tensor is still hard to be achieved, because of the approximations used for instance in the spin−orbit coupling operator.[5,16,20]

On the contrary, the g_{zz} value, as it may be expected from the previous section, appeared to be very sensitive to both the angle α and the bond distance d_{Cu-N}. This is especially apparent within the range of 120° < α < 160° and 1.75 Å < d_{Cu-N} < 1.85 Å, which corresponds to the most probable values of these parameters actually. By increasing with α and decreasing with d_{Cu-N}, the Δg_{zz} shift shows an opposite dependence with respect to these parameters, though the scope of the changes was less pronounced in the latter case (Figure 9). The reason for such reverse trend is immediately apparent from the inspection of Figure 3, which indicates that both variables, α and d_{Cu-N}, are mutually anticorrelated. Because of the high sensitivity of the Δg_{zz} to the angular orientation of the bound NO molecule, possible supramolecular interactions with the zeolite framework atoms on the opposite side of the channel wall in ZSM-5 may influence the Cu−N−O angle considerably. Therefore they

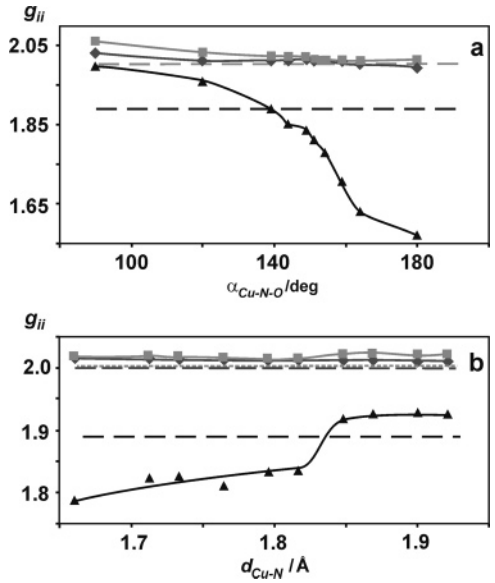

Figure 9. Dependence of the calculated ***g*** tensor (Pauli/VWN) components (-◆- g_{xx}, −■− g_{yy}, −▲− g_{zz}) on (a) the Cu−N−O bending angle (α) and (b) the copper−nitrogen distance (d_{Cu-N}) for the η^1{CuNO}^{11}/**M5(7)** cluster. The corresponding dashed lines indicate experimental values.

should be taken into account in a more advanced model.[10] This issue is now investigated in more detail both theoretically and experimentally, using zeolites with small cavities and narrow channels (such as LTA, RHO), which are able to enhance the molecular confinement of the η^1{CuNO}^{11} species. Taking into account the ambiguities and constraints discussed above we feel that significantly better agreement between calculated and experimental values than that shown in Table 2 could not be expected.

The results of our ***g*** tensor calculations nicely correspond to the speciation of the {CuNO}^{11} inside the ZSM-5 channels into two distinct complexes unraveled in high-field EPR experiments.[37] The lower values of the g_{zz} component were obtained for the **M5(7)** and **Z6** sites (located inside the main and the sinusoidal channels, respectively), whereas the **I2** sites being located in the channels' intersection give rise to the adducts with a higher value of the g_{zz} component. It was also found from our previous study[6] that the $^{Cu}a_{iso}$ isotropic coupling constants calculated for **M5(7)** and **I2** follow the same pattern. Thus, a higher g_{zz} value is associated with higher $^{Cu}a_{iso}$, and vice versa, in agreement with the EPR results.[37]

4. Conclusions

The ***g*** tensor components were satisfactorily reproduced within the spin-unrestricted GIAO-DFT method using a collinear ZORA/VWN approximation and TZP basis set for two types of zeolite clusters, accounting well for experimentally observed speciation of the copper nitrosyl adducts in the ZSM-5 zeolite. Magnetic properties of the η^1{CuNO}/ZSM-5 system can be explained within the concept of a η^1{CuNO}^{11} *magnetophore* perturbed by the nearest molecular environment. The calculated g_{xx} and g_{yy} components are relatively insensitive to the molecular geometry in contrast to the g_{zz}, which changes strongly with both the Cu−N−O angle and the Cu−N bond distance. Relativistic and diamagnetic contributions to the total ***g*** tensor shift, being similar in magnitude, are much smaller than the leading paramagnetic term. The different molecular origin of the ***g*** tensor of {q−NO}^{1}, η^1{CuNO}^{11}, and η^1{CuNO}^{11}/Z adducts is explained in terms of the magnetic field-induced couplings between the involved molecular orbitals. Whereas the g_{zz} value exhibits mainly an intraligand character, the g_{xx} and g_{yy} components are determined by the charge-transfer type couplings induced by the magnetic field. Both ***g*** and hyperfine coupling tensor calculations support speciation of the η^1-{CuNO}^{11} embedded within the ZSM-5 zeolite into two distinct complexes: one located inside the zeolite channels and the other at the channels' intersection.

Acknowledgment. Financial support by the Committee for Scientific Research of Poland, KBN, grant number 3 T09A 147 26, is acknowledged. The calculations were carried out with the computer facilities of CYFRONET-AGH, the Academic Computing Center, under grant number KBN/SGI2800/UJ/018/2002.

References and Notes

(1) Smyl, Y. *Carbon, Nitrogen, Sulfur: Human Interference in Grand Biospheric Cycles*; Plenum Press: New York, 1985; pp 115−250.
(2) Iwamoto, M.; Hamada, H. *Catal. Today* **1991**, *10*, 57.
(3) Spoto, G.; Bortiga, S.; Scarano, D.; Zecchina, A. *Catal. Lett.* **1992**, *13*, 39.
(4) Giamello, E.; Murphy, D.; Magnacca, G.; Morterra, C.; Shioya, Y.; Nomura, T.; Anpo, M. *J. Catal.* **1992**, *136*, 510.
(5) Neyman, K. M.; Ganyuszin, D. I.; Nasluzov, V. A.; Rösch, N.; Pöppl, A.; Hartman, M. *Phys. Chem. Chem. Phys.* **2003**, *5*, 2429.
(6) Pietrzyk, P.; Piskorz, W.; Sojka, Z.; Broclawik, E. *J. Phys. Chem. B* **2003**, *107*, 6105.
(7) Averill, B. A. *Chem. Rev.* **1996**, *96*, 2951.
(8) Ruggiero, C. E.; Carrier, S. M.; Antholine, W. E.; Whittaker, J. W.; Cramer, C. J.; Tolman, W. B. *J. Am. Chem. Soc.* **1993**, *115*, 11285.
(9) Schneider, J. L.; Carrier, S. M.; Ruggiero, C. E.; Young, V. G.; Tolman, W. B. *J. Am. Chem. Soc.* **1998**, *120*, 11408.
(10) Davidova, M.; Nachtigallova, D.; Nachtigall, P.; Sauer, J. *J. Phys. Chem. B* **2004**, *108*, 13674.
(11) Umamaheswari, V.; Hartmann, M.; Pöppl, A. *J. Phys. Chem. B* **2005**, *109*, 10842.
(12) Stone, A. J. *Proc. R. Soc. London, Ser. A* **1963**, *271*, 424.
(13) Keizers, C. P.; deBoer, E. *Mol. Phys.* **1974**, *29*, 1007.
(14) Lushington G. H.; Regin, F. *Int. J. Quantum Chem.* **1997**, *106*, 3292.
(15) Vahtras, O.; Minaev, B.; Aren, H. *Chem. Phys. Lett.* **1997**, *281*, 186.
(16) Neese, F.; Munzarova, M. L. In *Calculation of NMR and EPR Parameters. Theory and Applications*; Kaupp, M., Bühl, M., Malkin, V. G., Eds.; Wiley-VCH: Weinheim, Germany, 2004; p 21.
(17) van Lenthe, E.; Wormer, P. E. S.; van der Avoird, A. *J. Chem. Phys.* **1997**, *107*, 2488.
(18) Neyman, K. M.; Ganyushin, D. I.; Matveev, A. V. *J. Phys. Chem. A* **2002**, *106*, 5022.
(19) Schreckenbach, G.; Ziegler, T. *J. Phys. Chem. A* **1997**, *101*, 3388.
(20) Malkina, O. L.; Vaara, J.; Schimmelphennig, B.; Munzarova, M.; Malkin V. G.; Kaupp, M. *J. Am. Chem. Soc.* **2000**, *122*, 9206.
(21) Neese, F. *J. Chem. Phys.* **2001**, *115*, 11080.
(22) Patchkovskii, S.; Schreckenbach, G. In *Calculation of NMR and EPR Parameters. Theory and Applications*; Kaupp, M., Bühl, M., Malkin, V. G., Eds.; Wiley-VCH: Weinheim, Germany, 2004; p 505.
(23) Munzarova, M.; Kaupp, M. *J. Phys. Chem. A* **1999**, *103*, 9966.
(24) Schreckenbach, G.; Ziegler, T. *Theor. Chem. Acc.* **1998**, *99*, 71.
(25) te Velde, G.; Bickelhaupt, F. M.; van Gisbergen, S. J. A.; Fonseca Guerra, C.; Baerends, E. J.; Snijders, J. G.; Ziegler, T. *J. Comput. Chem.* **2001**, *22*, 931.
(26) Fonseca Guerra, C.; Snijders, J. G.; te Velde, G.; Baerends, E. J. *Theor. Chem. Acc.* **1998**, *99*, 391.
(27) ADF2004.01, SCM, Theoretical Chemistry, Vrije Universiteit, Amsterdam, The Netherlands (http://www.scm.com).
(28) van Lenthe, E.; Baerends, E. J.; Snijders, J. G. *J. Chem. Phys.* **1993**, *99*, 4597.
(29) van Wüllen, C. *J. Comput. Chem.* **2002**, *23*, 779.
(30) Delley, B. *J. Chem. Phys.* **1990**, *92*, 508.
(31) *DMol, InsightII*, release 2000.1; Accelrys Inc.: San Diego, CA, 2000.
(32) Becke, A. D. *J. Chem. Phys.* **1988**, *88*, 2547.
(33) Perdew, J. P.; Wang, Y. *Phys. Rev. B* **1992**, *45*, 13244.
(34) Vosko, S. H.; Wilk, L.; Nusair, M. *Can. J. Phys.* **1980**, *58*, 1200.
(35) Nachtigalova, D.; Nachtigal, M.; Sauer, J. *Phys. Chem. Chem. Phys.* **2001**, *3*, 1552.

(36) Sojka, Z.; Che, M.; Giamello, E. *J. Phys. Chem. B* **1997**, *101*, 4831.
(37) Umamaheswari, V.; Hartmann, M.; Pöppl, A. *J. Phys. Chem. B* **2005**, *109*, 1537.
(38) Hass, K. C.; Schneider, W. F. *J. Phys. Chem*. **1996**, *100*, 9292.
(39) Trout, B. L.; Chakraborty, A. K.; Bell, A. T. *J. Phys. Chem*. **1996**, *100*, 4173.
(40) Sierraalta, A.; Anez, R.; Brussin, M. R. *J. Catal*. **2002**, *205*, 107.
(41) Santiago, L. R.; Sierka, M.; Branchadell, V.; Sodupe, M.; Sauer, J. *J. Am. Chem. Soc.* **1998**, *120*, 1545.
(42) Sayle, D. C.; Richard, C.; Catlow, A.; Gale, J. D.; Perrin, M. A.; Nortier, P. *J. Phys. Chem. A* **1997**, *101*, 3331.
(43) Scheidt, W. R.; Ellison, M. K. *Acc. Chem. Res*. **1999**, *32*, 350.
(44) Boca, R. *Coord. Chem. Rev.* **1983**, *50*, 1.
(45) Arbuznikov, A. V.; Kaupp, M.; Malkin, V. G.; Reviakine, R.; Malkina, O. L. *Phys. Chem. Chem. Phys.* **2002**, *4*, 5467.
(46) Patchkovskii, S.; Ziegler, T. *J. Chem. Phys*. **1999**, *111*, 5730.
(47) Känzig, W.; Cohen, M. H. *Phys. Rev. Lett.* **1959**, *3*, 509.
(48) McGarvey, B. R.; Ferro, A. A.; Tfouni, E.; Bezerra, C. W. B.; Bagatin, I.; Franco, D. W. *Inorg. Chem*. **2000**, *39*, 3577.
(49) This picture is strictly valid at low temperatures such as liquid helium, where occupation of the $\Pi_{3/2}$ state is negligible. At higher temperatures the EPR spectrum could be obtained in the gas phase because of the low lying excited $\Pi_{3/2}$ state, see: Whittaker, J. W. *J. Chem. Educ.* **1991**, *68*, 421.
(50) Hoffman, B. M.; Nelson, N. J. *J. Chem. Phys*. **1969**, *50*, 2598.
(51) Freysoldt, C.; Pöppl, A.; J. Reinhold, *J. Phys. Chem. B* **2004**, *108*, 1582.
(52) Rudolf, T.; Pöppl, A.; Hofbauer, W.; Dieter, M. *Phys. Chem. Chem. Phys.* **2001**, *3*, 2167.
(53) Sojka, Z.; Pietrzyk, P. *Spectrochim. Acta A* **2004**, *60*, 1257.